The Science and Technologies for Fusion Energy With Lasers and Direct-Drive Targets

J. D. Sethian, D. G. Colombant, J. L. Giuliani, Jr., R. H. Lehmberg, M. C. Myers, S. P. Obenschain, A. J. Schmitt, J. Weaver, M. F. Wolford, F. Hegeler, M. Friedman, A. E. Robson, A. Bayramian, J. Caird, C. Ebbers, J. Latkowski, W. Hogan, W. R. Meier, L. J. Perkins, K. Schaffers, S. Abdel Kahlik, K. Schoonover, D. Sadowski, K. Boehm, L. Carlson, J. Pulsifer, F. Najmabadi, A. R. Raffray, M. S. Tillack, G. Kulcinski, J. P. Blanchard, T. Heltemes, A. Ibrahim, E. Marriott, G. Moses, R. Radell, M. Sawan, J. Santarius, G. Sviatoslavsky, S. Zenobia, N. M. Ghoniem, S. Sharafat, J. El-Awady, Q. Hu, C. Duty, K. Leonard, G. Romanoski, L. L. Snead, S. J. Zinkle, C. Gentile, W. Parsells, C. Prinksi, T. Kozub, T. Dodson, D. V. Rose, T. Renk, C. Olson, N. Alexander, A. Bozek, G. Flint, D. T. Goodin, J. Hund, R. Paguio, R. W. Petzoldt, D. G. Schroen, J. Sheliak, T. Bernat, D. Bittner, J. Karnes, N. Petta, J. Streit, D. Geller, J. K. Hoffer, M. W. McGeoch, S. C. Glidden, H. Sanders, D. Weidenheimer, D. Morton, I. D. Smith, M. Bobecia, D. Harding, T. Lehecka, S. B. Gilliam, S. M. Gidcumb, D. Forsythe, N. R. Parikh, S. O'Dell, and M. Gorensek

Manuscript received July 31, 2009; revised November 2, 2009. First published January 15, 2010; current version published April 9, 2010. This work was supported in part by the U.S. Department of Energy, by Department of Defense programs, Office of Defense Science and Inertial Fusion, National Nuclear Security Administration, and by the Office of Naval Research.

J. D. Sethian, D. G. Colombant, J. L. Giuliani, Jr., R. H. Lehmberg, M. C. Myers, S. P. Obenschain, A. J. Schmitt, J. Weaver, and M. F. Wolford are with the Plasma Physics Division, Naval Research Laboratory, Washington, DC 20375 USA.

F. Hegeler, M. Friedman, and A. E. Robson are with Commonwealth Technology, Inc., Alexandria, VA 22315 USA.

A. Bayramian, J. Caird, C. Ebbers, J. Latkowski, W. Hogan, W. R. Meier, L. J. Perkins, and K. Schaffers are with Lawrence Livermore National Laboratory, Livermore, CA 94550-9234 USA.

S. Abdel Kahlik, K. Schoonover, and D. Sadowski are with the Georgia Institute of Technology, Atlanta, GA 30332 USA.

K. Boehm, L. Carlson, J. Pulsifer, F. Najmabadi, A. R. Raffray, and M. S. Tillack are with the University of California, San Diego, La Jolla, CA 92093 USA.

G. Kulcinski, J. P. Blanchard, T. Heltemes, A. Ibrahim, E. Marriott, G. Moses, R. Radell, M. Sawan, J. Santarius, G. Sviatoslavsky, and S. Zenobia are with the University of Wisconsin—Madison, Madison, WI 53706 USA.

N. M. Ghoniem, S. Sharafat, J. El-Awady, and Q. Hu are with the University of California at Los Angeles, Los Angeles, CA 90095 USA.

C. Duty, K. Leonard, G. Romanoski, L. L. Snead, and S. J. Zinkle are with Oak Ridge National Laboratory, Oak Ridge, TN 37831 USA.

C. Gentile, W. Parsells, C. Prinksi, T. Kozub, and T. Dodson are with Princeton Plasma Physics Laboratory, Princeton, NJ 08543-0451 USA.

D. V. Rose is with Voss Scientific, Albuquerque, NM 87108 USA.

T. Renk and C. Olson are with Sandia National Laboratories, Albuquerque, NM 87185-1194 USA.

N. Alexander, A. Bozek, G. Flint, D. T. Goodin, J. Hund, R. Paguio, R. W. Petzoldt, D. G. Schroen, and J. Sheliak are with General Atomics, San Diego, CA 92121 USA.

T. Bernat, D. Bittner, J. Karnes, N. Petta, and J. Streit are with Schafer Corporation, Livermore, CA 94551 USA.

D. Geller and J. K. Hoffer are with Los Alamos National Laboratory, Los Alamos, NM 87545 USA.

M. W. McGeoch is with PLEX Corporation, Brookline, MA 02146 USA.

S. C. Glidden and H. Sanders are with Applied Pulsed Power, Inc., Freeville, NY 13068-0348 USA.

D. Weidenheimer, D. Morton, and I. D. Smith are with L3 Pulse Sciences, Inc., San Leandro, CA 94577-5602 USA.

M. Bobecia and D. Harding are with the Laboratory for Laser Energetics, University of Rochester, Rochester, NY 14623-1212 USA.

T. Lehecka is with the Penn State Electro-Optics Center, State College, PA 16229 USA.

S. B. Gilliam, S. M. Gidcumb, D. Forsythe, and N. R. Parikh are with The University of North Carolina at Chapel Hill, Chapel Hill, NC 27514 USA.

S. O'Dell is with Plasma Processes, Inc., Huntsville, AL 35811-1558 USA.

M. Gorensek is with Savannah River National Laboratory, Aiken, SC 29808 USA.

Digital Object Identifier 10.1109/TPS.2009.2037629

***Abstract*—We are carrying out a multidisciplinary multi-institutional program to develop the scientific and technical basis for inertial fusion energy (IFE) based on laser drivers and direct-drive targets. The key components are developed as an integrated system, linking the science, technology, and final application of a 1000-MWe pure-fusion power plant. The science and technologies developed here are flexible enough to be applied to other size systems. The scientific justification for this work is a family of target designs (simulations) that show that direct drive has the potential to provide the high gains needed for a pure-fusion power plant. Two competing lasers are under development: the diode-pumped solid-state laser (DPPSL) and the electron-beam-pumped krypton fluoride (KrF) gas laser. This paper will present the current state of the art in the target designs and lasers, as well as the other IFE technologies required for energy, including final optics (grazing incidence and dielectrics), chambers, and target fabrication, injection, and tracking technologies. All of these are applicable to both laser systems and to other laser IFE-based concepts. However, in some of the higher performance target designs, the DPPSL will require more energy to reach the same yield as with the KrF laser.**

***Index Terms*—Fusion power generation, fusion reactors, laser amplifiers, laser fusion, magnetic fields, nanotechnology, optical tracking.**

I. Introduction

WE ARE carrying out a multidisciplinary multi-institutional program to develop the scientific and technical basis for the direct-drive approach to laser fusion energy. In this approach an array of lasers directly illuminates a cryogenic capsule (3–5-mm diameter) containing frozen deuterium–tritium that has been injected into a reaction chamber. The capsule is compressed and heated to fusion ignition and high gain. The fusion energy is absorbed by the chamber wall and blanket and then converted into electricity and, possibly, hydrogen. The process is repeated at a repetition rate of about 5 Hz. Some of the advantages of this approach to fusion energy are as follows.

1) Direct drive has the simplest target physics. The main concern is hydrodynamic instability, which appears to be resolved with a combination of advances in laser

technology and target design. Other issues such as laser–target coupling and suppression of laser–plasma instabilities (LPI) can be and are being addressed on subscale experiments.

2) Direct drive is best suited for energy production. It has the promise of power-plant-level pure-fusion gains with relatively modest laser energies: around 1 MJ with conventional direct drive, or as low as 500 kJ with "shock ignition," as described in this paper.
3) Vast physics base: The scientific underpinnings for laser fusion are well established due to the work in the inertial confinement fusion (ICF) program carried out by the U.S. National Nuclear Security Administration and international efforts. Note that the National Ignition Facility (NIF) will use the indirect-drive approach for the first laboratory demonstration of thermonuclear ignition. This approach, where laser light is converted to X-rays that drive the target, was chosen based on the primary mission of the NIF to study weapon physics. However, much of the underlying physics applies to the direct-drive approach.
4) The laser, the most costly component (about one-third of the cost of the plant [1]), is modular. In most reactor designs, the laser is composed of 20–60 identical beam lines. Thus, all the development can be done on one laser beam line, which, when perfected, is then replicated to build the entire laser system. This lowers development costs and risk.
5) Direct-drive targets are the simplest to manage. They are spherically symmetric shells that have been fabricated in a droplet generator, they require no preferred direction of illumination, and they have no hohlraum debris to recycle.
6) The main components are physically separated from the reaction chamber. Thus, they can be developed separately before they are integrated into the system. This also reduces development costs. Just as importantly, it allows economical upgrades.
7) Power-plant studies show that the concept is economically attractive [1], [2].

Our "business model" develops the key components for inertial fusion energy (IFE) as a coherent integrated system, simultaneously developing the needed science, technology, and engineering and always linking them to the final application of an attractive power plant. We leverage heavily off the target physics, laser development, and target fabrication technologies developed in the ICF program, and the materials and reactor technologies developed in the magnetic fusion energy (MFE) program.

This paper describes some of the recent progress in developing the key components. A description of earlier progress is given in the literature [3]. We start with a brief overview of the direct-drive target designs and then present the status of the two candidate laser systems: the diode-pumped solid-state laser (DPPSL), operating at the third harmonic with a wavelength of 351 nm, and the electron-beam-pumped krypton fluoride (KrF) gas laser, operating at its fundamental wavelength of 248 nm. We follow with a description of the progress made in the other components: final optics (grazing incidence and dielectric mirrors); target fabrication, injection, and tracking technologies; and the development of the reaction chamber.

II. Target Design

The scientific justification for this paper is a family of target design simulations from several institutions that show that direct drive has the potential to provide the high gains needed for a power plant based on pure-fusion energy [4]. The required gain is determined by the typical metric for an inertial-fusion power plant: $\eta G > 10$, where η is the laser efficiency and G is the target gain. KrF lasers have a projected efficiency (wall plug to light on the target) of around 7%. Thus, the target gain needs to be in excess of 140. DPPSLs might be able to exceed 10% (at 351 nm), which would lower the gain requirement to 100. Obviously, the higher the gain the better, because it not only decreases recirculating power, it also provides a cushion in the target design to allow for real-world asymmetries, variations, etc. The following three types of target designs are considered.

1) Conventional direct-drive designs, with implosion velocities of 300 km/s. These are applicable to both KrF and DPSSL lasers and show power-plant-class gains (> 140) at laser energies around 2.4 MJ [5], [6].
2) High-velocity (350–400-km/s) direct-drive designs that take advantage of the deeper UV of a KrF laser. Codes predict gains > 50 at 500 kJ and > 140 (i.e., needed for energy) around 1 MJ [7]. These are referred to as Fusion Test Facility (FTF) designs.
3) "Shock ignition" designs have the prospect of requiring only submegajoule (KrF) lasers for a power plant. In shock ignition [8], a short high-intensity laser pulse applied near peak compression drives a high-intensity shock to ignite the target. Shock ignition requires lower velocity implosions than conventional direct drive (200–250 versus 300–400 km/s). Shock ignition will provide similar enhancement in DPSSL-based systems; however, the driver energy needs to be higher to reach equivalent target yield to KrF.

The gain curves for the three targets are shown in Fig. 1. Higher performance (gain) is predicted at lower laser energy for a KrF ($\lambda = 248$ nm) than a DPPSL ($\lambda = 351$ nm). This is because the shorter wavelength of KrF both maximizes the coupling efficiency and increases the threshold of LPIs. The latter means that a KrF target can be driven to higher implosion velocities at lower laser energies. Alternatively, the KrF target can be driven with higher pressures and hence have better hydrostability.

KrF lasers also produce the smoothest laser beam. A technique called induced spatial incoherence (ISI) [10], [11] produces very high quality focal profiles ($< 0.2\%$ spatial nonuniformities). That smoothness, coupled with the high bandwidth ($\sim$3 THz), minimizes laser-induced perturbations or "imprinting" on the target. A beam-smoothing technique called smoothing by spectral dispersion (SSD) [12], [13] can effectively be applied to a DPPSL. While SSD does not

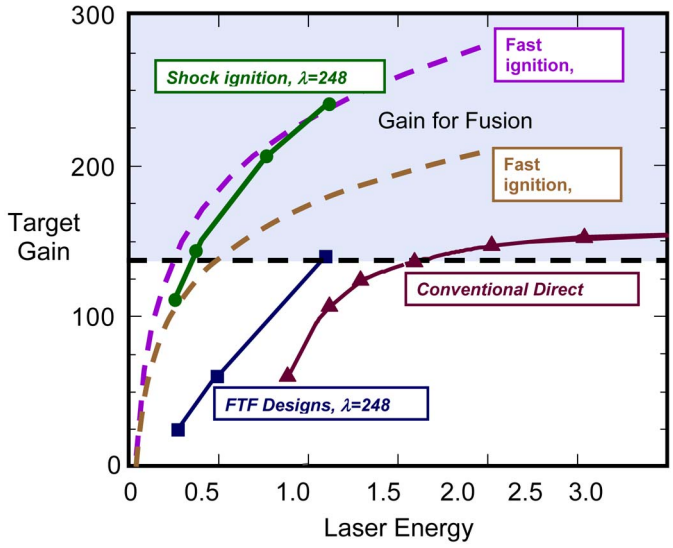

Fig. 1. Gain curves from 1-D simulations of various high-performance direct-drive target designs. The shaded region shows sufficient gain for the pure-fusion power plant. (Triangles) Conventional direct drive, KrF, or DPPSL (300-km/s implosion velocity). (Squares) FTF designs for KrF $\lambda = 248$ nm) and higher ablation pressure implosion velocity of 350–450 km/s. (Circles) Shock ignition targets for KrF: Soft conventional compression (< 300 km/s) and then spike to shock heat to ignition. (Dashed lines) Fast ignition scaling [9] for KrF (248 nm) and DPPSL (351 nm).

produce as smooth a focal profile in all modes as ISI, it should be adequate for the conventional high-gain target designs [14].

The net effect of all the advantages of KrF is illustrated with one point design for a shock ignition target [4]. The gains are predicted to be 92 with a 230-kJ KrF laser and 55 with a 450-kJ glass laser. The predicted fractions of incident laser light coupled to the target are about 77% for a KrF laser and about 55% for a DPPSL. These calculations assume that the laser is "zoomed," i.e., the spot size is decreased to follow the imploding pellet. Zooming increases the coupling efficiency by about 35%. Note that shock ignition predicts comparable performance to fast ignition but does so without the need for complex targets and an additional more challenging type of laser.

The curves in Fig. 1 are a compilation of 1-D target simulations. Full 2-D simulations have been carried out for most of these designs. For example, 2-D simulations of shock ignition targets, which incorporate realistic nonuniformities in the target surface or laser, generally show about 65%–80% of the gain predicted in one dimension [4].

The codes used to generate the gain curves in Fig. 1 have been benchmarked against experiments with planar target experiments that are within two to five times of the prototypical laser fluence (2–3 kJ in 750-μm-diameter spot). While the hydrodynamic stability of these targets has been fairly well established with a combination of simulations, experiments, and advances in target design and laser technologies, one area that is difficult to predict is the effect of LPI. Any laser–target design is subject to LPI. These laser-driven instabilities occur in the ablated plasma surrounding the pellet. LPI can produce high-energy electrons that can preheat DT fuel, which lowers the final density and, hence, fusion gain. LPI can also scatter the laser beam, which reduces the drive efficiency. LPI is less of a concern with shorter wavelength lasers because the threshold is higher. The ponderomotive force driving LPI goes roughly as $I\lambda^2$, where I is the intensity and λ is the wavelength. Thus, KrF with its shorter wavelength (248 nm) should be more resistant to LPI than a DPPSL (351 nm). The experiments on the Nike KrF laser at the Naval Research Laboratory (NRL) have born this out [15]: The onset of LPI, as witnessed by the detection of hard X-rays and scattered light, occurs at 1.7×10^{15} W/cm^2. In contrast, the LPI threshold for a glass laser operating at 351 nm is typically between 0.5 and 1.0×10^{15} W/cm^2. (It should also be noted that a glass laser not only has a lower LPI threshold but also requires more intensity to apply the same ablation pressure as KrF.)

The KrF intensities required to achieve the high implosion velocities in the FTF class targets, as well as those required in the main drive of the shock ignition targets, range from 1.0 to 2.0×10^{15} W/cm^2. While many factors are in play here, it appears that the target requirements are below the observed KrF LPI threshold. Further experiments are being carried out to fully explore this region. On the other hand, the intensity of the spike in the shock ignition designs is around 2×10^{16} W/cm^2 or well above the LPI threshold. However, LPI may not be an issue because the shock is applied late in time. The core is already compressed, so preheat is not an issue. Moreover, simulations suggest that these "late" hot electrons, if they have energies below 100 keV, will be stopped by the outer surface of the dense compressed core and may result in a more efficient heating mechanism [8].

III. Lasers

Both KrF and DPPSL have the potential to be viable candidates for a fusion energy system. KrF laser development is carried out primarily with the Electra laser at NRL, whereas DPPSL development has been carried out with the Mercury laser at LLNL. Both are developing technologies that are scalable to power-plant-size systems. Both have the potential to meet the fusion energy requirements for cost, although a high-confidence estimate of the cost cannot be made until the technology is fully developed. KrF is a gas laser that is pumped with high-voltage high-current electron beams (500–800 keV and 100–500 kA). DPPSLs are solid-state lasers that are pumped with an array of high-efficiency ($> 60\%$) high-power ($>$ 100-W) diodes. The medium is Yb:S-FAP, but other media, including the NIF choice of Nd:glass, are under consideration. The fundamental wavelength is 1051 nm, but they can be tripled to 351 nm with 70% efficiency.

The Electra KrF laser runs at 2.5–5 Hz and produces between 300 and 700 J in an oscillator mode. Based on development of the individual components, a fusion-energy-class KrF laser is predicted to have a wall plug to laser light on target efficiency in excess of 7%. Recent advances have dramatically increased the lifetime of the thin foil that separates the electron-beam diode from the laser gas. Eliminating voltage reversals after the main power pulse prevents localized high-current emission that can melt pinholes into the foil. Electra has run 90 000 shots continuously at 2.5 Hz (10 h) and 50 000 shots in two runs at 5 Hz. Over 320 000 laser shots were taken in an eight-day period. The continuous run lifetime is now largely limited by

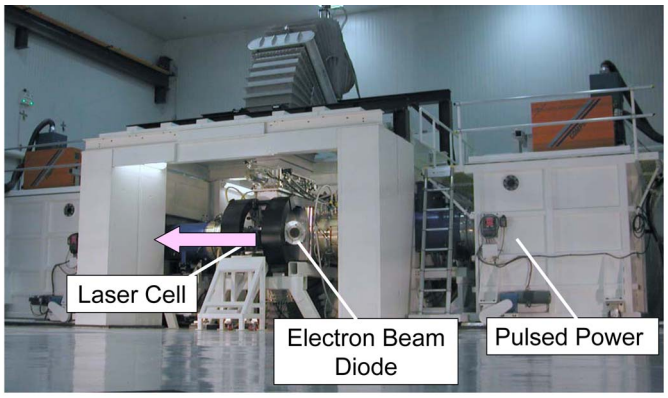

Fig. 2. NRL's electron-beam-pumped Electra KrF laser system. The laser output window is between the two black magnet coils in the center of the photograph. The arrow shows the laser path. The magnets guide the electron beams into the laser gas. The pulsed-power systems for the electron beams consist of the blue pulse-forming lines and the attendant white tanks that flank the laser cell.

erosion of the spark-gap-based pulsed power that drives the electron beams. An all-solid-state pulsed-power system has been built using components that have demonstrated lifetimes in excess of 300 000 000 shots. This integrated 180-kV demonstrator module has run continuously at 10 Hz for over 11 500 000 shots ($>$ 13 days) and will become the basis for a system to be deployed on Electra. More details on Electra technology and its performance can be found in [16]–[18]. A photograph of Electra appears in Fig. 2.

The Mercury DPPSL has produced greater than 50 J of laser light (1051 nm) for over 300 000 shots in a series of runs of 0.5–2 h at a repetition rate of 10 Hz. The overall efficiency of a DPPSL-based system is projected to be 10% (at the fundamental wavelength). Many advanced technologies have been developed for Mercury, including high-power diode arrays, forced gas cooling of the laser crystal, high-power (200-W) Pockels cells, adaptive optics, and high-efficiency frequency conversion to the third harmonic. The high-power diode lifetime has been demonstrated to be over 140 000 000 shots. A smaller front end for Mercury that uses the same diode/crystal architecture was recently completed and produces 500 mJ. It has run for well over 10 000 000 shots with an rms stability of 0.78%. A photograph of the Mercury laser appears in Fig. 3. Further details can be found in [19]–[21].

In weighing the merits of these two approaches, they both warrant continued development. KrF has significant inherent physics advantages for driving high-gain fusion-energy-class targets, as described in Section II. Thermal management is easier on account of the gas laser medium. Zooming is straightforward with KrF and has been demonstrated by means of an optical switchyard that progressively routes the laser through decreasing apertures [22]. The switchyard is located in the low-energy front-end laser that feeds all the amplifiers. However, when viewing fusion energy as a complete system, DPPSLs are a viable choice because of the longer wavelength, which reduces optics damage considerations, the potential for higher wall plug efficiency, and the higher durability expected from an all-solid-state system. In addition, the cost of DPPSLs may be reasonable if current projections hold true that the price of the laser diodes (the most costly components in the system) will drop significantly in the next 10–12 years.

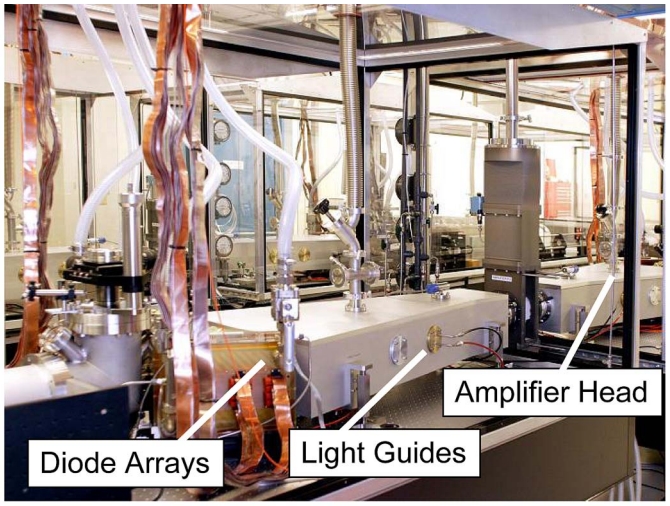

Fig. 3. Close-up view of the LLNL Mercury DPPSL. In the foreground is one of the two amplifiers. The diode arrays are located at the ends of the two trapezoidal light guides. The amplifier head, including the crystal, is located in the white cylinder between the two guides. The light from the diodes is focused onto the crystal from both sides.

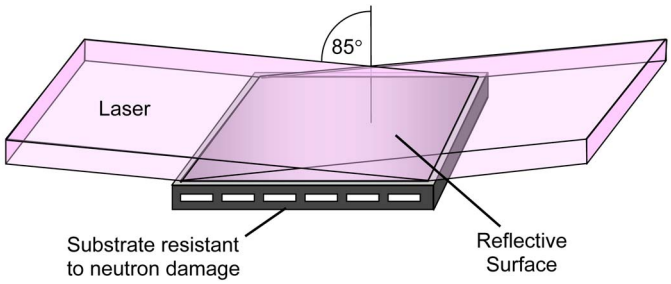

Fig. 4. GIMM concept.

IV. Final Optics

The final optics transport the laser beams to the reaction chamber center. They are the only optics to see the direct emissions from the target. The front-runner final-optic concept is a grazing incidence metal mirror (GIMM), as shown in Fig. 4.

This was first proposed in response to concerns over radiation damage to multilayer dielectric mirrors [23]. The decision to develop the GIMM is based on its potential for high laser damage threshold, its ability to withstand some uniform erosion, its simplicity, and its applicability to both KrF and DPPSL wavelengths. For example, the reflectivity at normal incidence is about 93% at both 248- and 351-nm wavelengths [24]. The GIMM would consist of an aluminum–alloy surface bonded to a cooled substrate that is resistant to neutron swelling (e.g., aluminum, AlBeMet, or, possibly, SiC). Operation at a shallow angle ($\sim 85^\circ$) with s-polarized light gives higher reflectance ($> 99\%$), hence less energy absorbed by the mirror. It also lowers the average fluence on the surface due to the larger beam footprint.

Experiments were conducted to determine the damage threshold using a homogenized KrF laser: 700 mJ, 25 ns, and 100 Hz. Damage was detected with a high-speed vision system

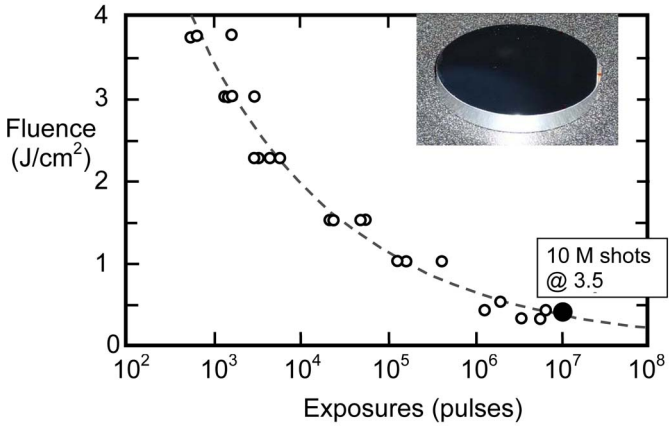

Fig. 5. Observed laser damage threshold for various Al and Al alloy mirrors. The smaller color circles represent various alloys or deposition techniques. The highest performance was achieved with an Al–5% Cu solid solution alloy, as marked by the large filled circle. That point does not represent a damage limit but rather marks the end of that test.

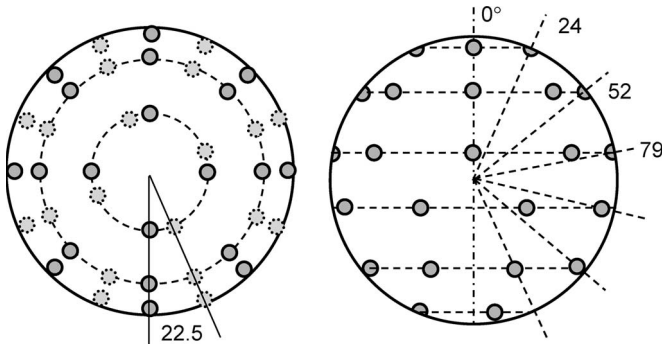

Fig. 6. Views of entry points on a sphere for 40-beam illumination. (Left) View from the top of the sphere. The small dotted circles correspond to the ports on the lower half. (Right) Side view.

that images scattered light under the footprint of the main laser that results from both the laser itself and a HeNe probe laser. The main laser is allowed to fire only when the vision system indicates that the amount of scattered light is below an empirically established threshold. The reflectivity of the mirror does not change until damage is detected. As shown in Fig. 5, this type of mirror can resist at least 3.5 J/cm^2 for more than 10 000 000 shots [25].

The highest laser intensity survived to date was achieved with an Al–5% Cu solid solution alloy. Note that this is not a damage point but rather the highest fluence that could be applied with the homogenized beam.

Based on the previous results, we have designed a final-optic train that can meet the requirements for illumination uniformity, adequate tritium breeding, GIMM damage threshold, and neutron damage. The configuration is shown in Fig. 6. It was developed for the "conventional direct-drive" target and is applicable to both DPPSLs and KrF. The chamber has 40 beam ports, which are adequate for the illumination uniformity required by the target physics [26], [27]. The 40 beam ports are arranged in six azimuthal tiers. There are four ports in the 24° tier (with 0° being defined as the pole) and eight ports in each of the 52° and 79° tiers. Thus, the total number of ports is 20 in the upper hemisphere and 20 in the lower

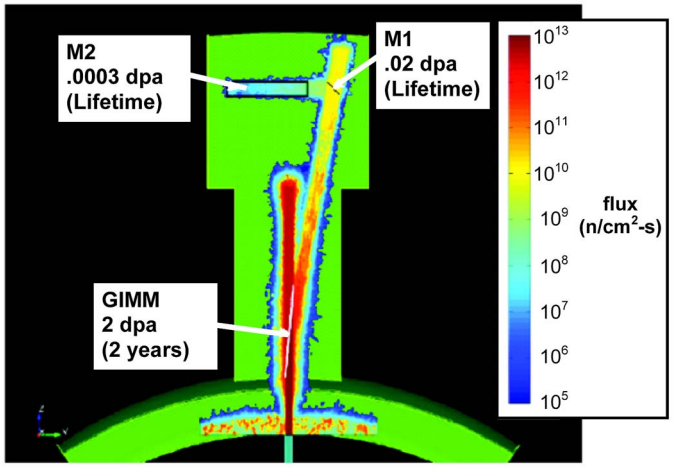

Fig. 7. Final-optic assembly showing the GIMM, the two dielectric mirrors M1 and M2, and the predicted neutron flux on optical components. The plant "Lifetime" is assumed to be 30 years.

hemisphere. The lower sets of ports are offset by 22.5° from the corresponding upper ones so as to avoid any beam pointing into an opposing beam, which carries a risk of optical damage if the target is not hit squarely. Note that the poles are left open for target injection/tracking, and the equatorial belt is left open for a magnetic intervention dump, as discussed in Section VI on reaction chambers. Other configurations are possible.

The GIMM is located in its own shielded housing at a distance of 24 m from the target. Each GIMM consists of 50 separate elements, or GIMMlets, with dimensions of 15 cm high $\times$ 172 cm wide, and arranged in a 2 $\times$ 27 array. Thus, the entire GIMM is 3.44 m high $\times$ 4.05 m wide. The final-optic assembly is shown in Fig. 7, which also shows the predicted neutron flux and displacements per atom (dpa) for the power-plant lifetime.

The neutron flux was calculated using a newly developed tool that directly couples a CAD-based engineering package with a neutronics code called Direct Accelerated Geometry MCNP [28]. This allows preservation of details with complex surfaces without a need for geometry simplification.

The simulation shows that the GIMM scatters a significant number of neutrons onto the dielectric mirrors over the 30-year projected life of the plant. In keeping with the earlier concern that dielectrics may not be able to withstand this level of neutron fluence, we carried out a series of tests on dielectric materials. The hypothesis was that we could avoid the damage seen in previous studies if we matched the neutron-induced swelling in the substrate with that in the mirror layers. Three different dielectric stacks (mirror systems) were exposed at prototypical neutron fluence and temperature using the Oak Ridge National Laboratory (ORNL) HFIR.

After exposure, the samples showed no visible signs of surface abrasion, film delamination, cracking, or pitting. They did show an apparent darkening that increased with increasing neutron dose. Independent of this darkening, the samples showed virtually no change in reflectivity: The reflectivity results for one of the samples (Al_2O_3/SiO_2) are shown in Fig. 8 [29]: While the peak wavelength has shifted slightly, which is to be expected as the layers compact slightly under irradiation,

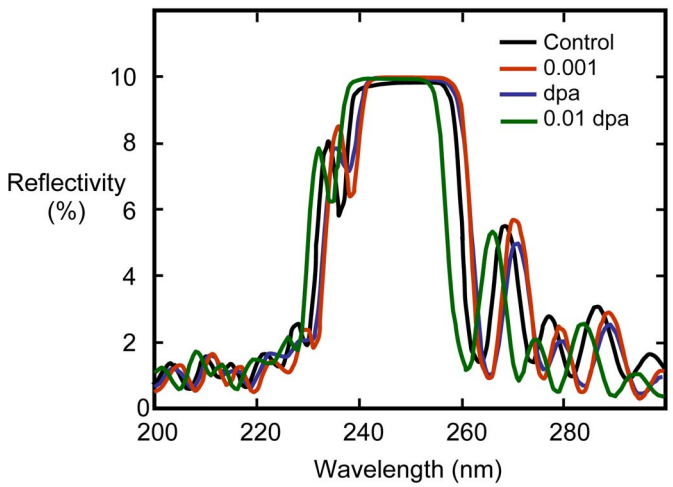

Fig. 8. Reflectivity of (Al_2O_3/SiO_2) dielectric mirror stack after exposure to neutrons from the ORNL HFIR.

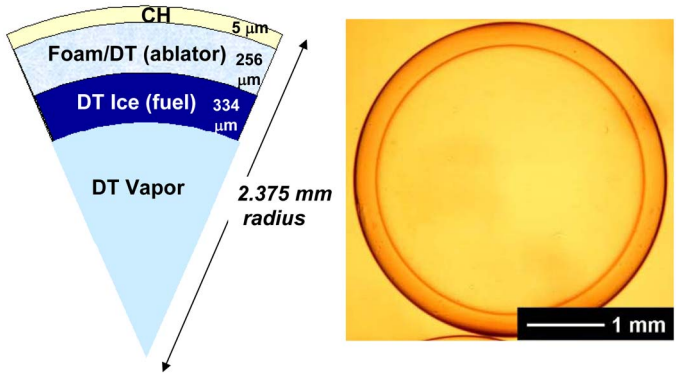

Fig. 9. (Left) Buildup of a high-gain target. The dimensions and aspect ratio vary for the various target designs, but the constituents are the same. (Right) Image of a foam shell in an index-matching solution.

there is virtually no change in reflectivity, even at 0.1 dpa, or roughly five times the predicted service life of the mirror. These samples were also tested for laser damage threshold. Within the error of measurement, no change in laser damage threshold was detected, even at 0.1 dpa [30].

V. Target Fabrication

The buildup of all the high-gain direct-drive targets described in Section 1 is shown in the left-hand side of Fig. 9. The right-hand side shows an image of a 4-mm-diameter divinylbenzene (DVB) foam shell in an index-matching solution. Such a shell would form the second layer in the target.

Recent progress toward fabricating these targets include the following.

1) A method to apply an Au–Pd alloy coating on the target. This coating serves three functions: It helps the target physics as it provides a soft X-ray drive during the beginning of the pulse [31], it allows fast DT permeation times, and it provides a reflective IR layer that helps prevent the cryogenic target from warming above melting as it traverses the hot chamber.
2) Mass production of both divinylbenzene and resorcinol formaldehyde foam shells that meet the target specifications for diameter, density, sphericity, and nonconcentricity (NC). These are made in a droplet generator that can produce up to 22 shells/min and can control the diameter to within 1% [32].
3) A cost estimate of \$0.16 each for mass production and injection of these targets [33]. This analysis was based on a chemical engineering analysis of all the process steps and assuming a commercial process plant environment. This is under the \$0.25 cost requirement cited by the Sombrero study [1].
4) Demonstration that ultrasmooth DT ice layers can be grown over a foam underlay and that these ice layers remain sufficiently smooth at temperatures as low as 16 K [34]. This aids target survival during injection into the chamber. The target can be injected at a colder temperature and allowed to warm up without either compromising the layer smoothness, or exceeding the DT melting point of 19.3 K.
5) Fabrication of a fluidized bed to demonstrate an ultrasmooth DT ice surface (cryolayering) on a mass production basis [35]. Smoothing has been successfully demonstrated with a room-temperature surrogate and will now be extended to cryogenic targets. The work is supported by an extensive modeling effort [36].

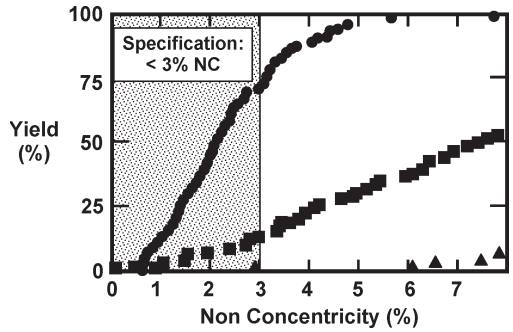

Fig. 10. Improvement in yield of shells that meet NC specifications. The triangles correspond to the earliest attempts at DVB shells, the squares to the best results with resorcinol–formaldehyde shells, and the circles with the newest formulation of DVB shells.

The two major remaining tasks, in addition to the development of mass production cryogenic layering, are to develop a technique to apply a thin overcoat to the foams (to provide a seal coat for the DT) and to improve the yield of the foam shells that meet NC specifications.

We have already demonstrated that an overcoat can be applied to a foam shell by either interfacial polymerization, glow discharge polymerization, or a combination of these. The issue is that current coatings need to be 10–15 μm thick to have the needed high integrity, whereas the target physics calls for only 1–2 μm. One promising approach has been the application of a thin solid coat on both DVB and RF foam shells during the gelation phase [37], [38].

The mass-produced foam shells tend to meet all the specifications except NC. The NC specification, which can also be viewed as a variation in wall thickness, is less than 3% and preferably less than 1%, depending on how robust a target design is needed. Fig. 10 shows that the yield has been increasing

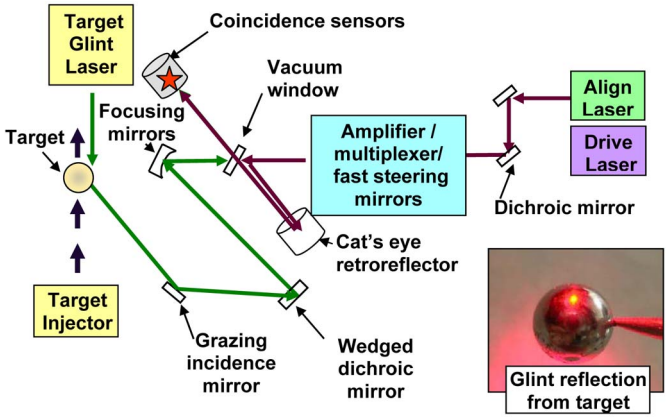

Fig. 11. Schematic of the "glint" system to perform the final mirror steering to engage the target. The inset shows a photograph of the glint off the target.

from virtually zero to over 60% as new foam chemistries and protocols are being developed [39].

Another approach to fabricating foam shells is the use of microfluidics and electrophorisis to manipulate and form the foam into shells while still in its liquid phase [40], [41].

VI. Target Engagement

At first glance, precisely illuminating a pea-sized cryogenic target that is injected into the center of a 10–22-m-diameter reaction chamber would seem to be a rather daunting task. Particularly considering that the required illumination precision is 20 μm (rms between the centerline of laser beamlets to the centerline of the target). However, we have developed a concept and performed a successful proof-of-principle bench test to show that it is feasible [42]. The concept is based on a four-stage process. The first stage employs optical sensors that precisely determine the target's diameter and launch velocity. The second stage, encompassing most of the target's trajectory, employs a separate optical sensor that continuously monitors lateral deviations of the target's trajectory. In the third stage, immediately prior to arrival at the chamber center, the target is illuminated by a short-pulse low-intensity "glint" laser. The glint returns utilize the same optics as each beamlet, except that the glint passes through a monolithic wedge dichroic mirror. This compensates for the target motion after the glint and the offset between the glint position and the target center. In the fourth stage, the fast-steering mirrors in the drive laser beam lines aim each drive beamlet to the position of the glint return. The beamlets then reflect off the front surface of the wedge to engage the target. A drawing of this fourth stage is shown in Fig. 11.

We have demonstrated each stage of this process using a surrogate target (4-mm stainless-steel BB) falling at 5 m/s under vacuum [43]. Optical measurements made with a pair of crossing sensors predict the time the target will arrive within the $\pm$1-mm field of view assigned to the glint sensor. If the target cannot be regularly placed within the 1-mm field of view, lateral excursions during its trajectory can be monitored and the field of view can be adjusted accordingly. These excursions are monitored by a Poisson spot tracking system in which an axial laser beam creates a bright diffraction spot at the precise center of the target's shadow. (The measured precision relative to a 4-mm target at the center of a simulated 14-m chamber is 4 μm and updated every 3 ms.) Thus, these position measurements allow the fast-steering mirror to apply most of its angular correction during a period in excess of 100 ms rather than the few milliseconds it takes for the target to reach the chamber center after being illuminated by the glint system (1–2 ms in a full-size IFE chamber). The precision with which the glint offset can be measured with its camera sensor is 4 μm.

Our target engagement verification technique utilizes a simulated driver beam diameter that is larger than the target and produces a sharply focused halo around the target's shadow. A camera is used together with an edge-finding algorithm to measure the centroid separation between the inner and outer boundaries of the halo. The measured verification error for a fixed target is 4 μm. Currently, the engagement accuracy for moving targets is 34 μm rms. We anticipate with further improvements (e.g., reducing the electrical noise associated with the steering mirrors) that the total error in our demonstration will be less than the 20-μm requirement.

Most of the remaining error is from sources that are expected to scale well to the increased distances required for IFE. The effect of fast-steering mirror electrical noise beam position is proportional to the maximum absolute distance through which the beam must be steered ($\pm$1–2 mm in our experiment and in a power plant). For the "glint" position measurements, the precision in sensor space is simply a function of the intervening optical magnification (assuming insignificant gas density variations and no high-frequency vibrations of the optics), which can be preserved in a full-scale system.

The system has been designed assuming an injection velocity of 50 m/s. Higher injection velocity will obviously require faster position measurements and more rapid mirror positioning.

VII. Reaction Chamber

The reaction chamber is one of the most challenging aspects in developing any practical fusion power plant. It is no different for laser fusion. The first wall (FW) of the reaction chamber must withstand the steady pulses of X-rays, ions, and neutrons from the target, must allow high-efficiency transport of the deposited energy to the electrical generator, and must allow sufficient neutron transport to the tritium breeding blanket. One advantage that IFE has over an MFE system is that the emissions emanate from a point source away from the wall, so one can exploit $1/r^2$ scaling to reduce the wall loading. On the other hand, one disadvantage that IFE has over MFE is that the emissions are pulsed, so the instantaneous thermal loading can be several orders of magnitude higher.

In designing the chamber FW, it is necessary to calculate first the emission or "threat" spectrum from the target. Table I gives the energy accounting, 100 ns after burn, of all the constituents of a high-gain conventional direct-drive target. In this case, approximately 1.3% of the energy is released in X-rays (surface deposition, < 1 μm), 24% in ions (subsurface deposition, < 5 μm), and the remainder in neutrons (volumetric deposition) [44]. This ratio is representative of all direct-drive target designs.

TABLE I
ENERGY ACCOUNTING FROM A HIGH-GAIN TARGET (LASER ENERGY OF 2.46 MJ AND GAIN OF 150)

	Thermal Debris (J)	Burn and Nuclear Products (J)	Total (J)
X-rays	–	–	4.937e6
Gammas	–	1.680e4	1.680e4
Neutrons	–	2.743e8	2.743e8
Protons	6.255e5	1.137e6	1.763e6
Deuterons	1.166e7	1.006e7	2.1724e7
Tritons	1.733e7	9.166e6	2.650e7
^{3}He	3.171e4	4.607e4	7.777e4
^{4}He	3.556e6	2.673e7	3.028e7
^{12}C	6.879e6	8.834e2	6.880e6
^{13}C	8.366e4	1.141e1	8.367e4
Pd	1.844e5	<1	1.844e5
Au	3.607e5	<1	3.607e5
Pt	<1	<1	<1
	4.071e7	**3.214e8**	**3.671e8**

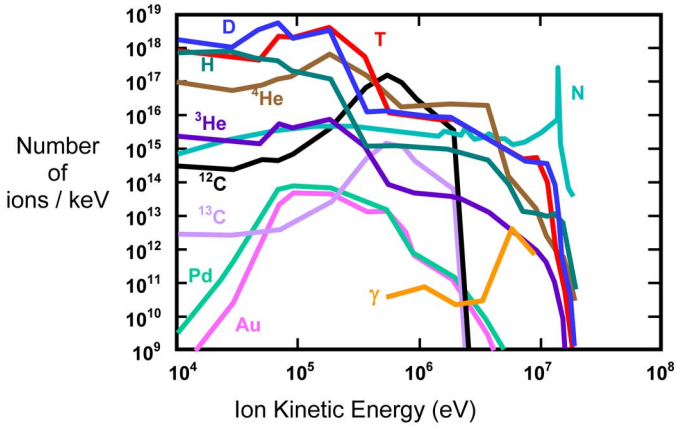

Fig. 12. Threat spectra from the conventional direct drive shown in Table I.

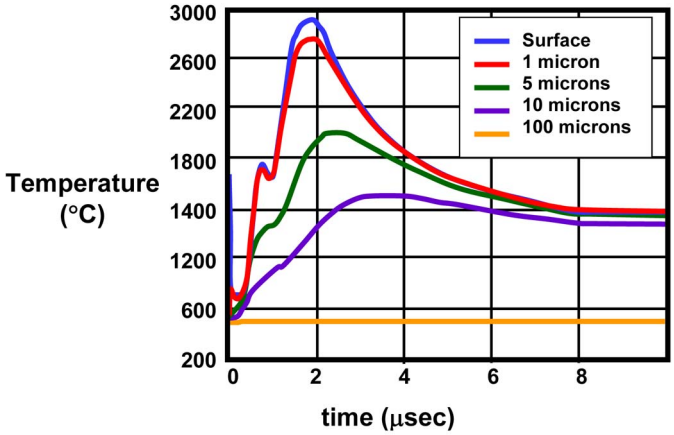

Fig. 13. Representative temperature history of the FW as a function of depth from the surface. This is for a tungsten-armored FW, at a radius of 6.5-m fusion yield of 154 MJ, and no gas inside the chamber. The details of the curves will differ as the target yield and/or chamber radius is changed, but the basic behavior is the same.

Fig. 12 shows the ion and neutron spectra from the target. Pd and Au are in a thin layer to help the target performance, as described in Section V.

The two physical processes of greatest concern are cyclic thermal loading and helium retention. Both of these can severely degrade the thermomechanical properties of the FW material. As in any fusion reactor, neutron damage is also a consideration and needs to be addressed. However, that is on a much longer damage cycle than the phenomena discussed here.

Cyclic thermal loading leads to stress-driven crack growth in the FW. Fig. 13 shows the temperature history of the wall as a function of depth [45]. This is for a target yield of 154 MJ, a tungsten-armored FW at a radius of 6.5 m, and an initial wall temperature of 600 °C. Note that the temperature is highest within the first few micrometers. This is a direct consequence of the short penetration depth of the ions, their relatively short pulsewidth, and the fact that the ions carry a relatively high fraction of the reaction energy. The key concern with respect to these temperature histories is cracking in tungsten, although as discussed below this appears to be manageable [46].

Helium retention is the more insidious problem. Because the helium migration distance is much shorter (50–100 nm) compared to the implantation distance (2–5 μm), helium tends to coalesce into bubbles and at grain boundaries. The resulting buildup in helium pressure exfoliates the surface. This is a well-known phenomenon [47].

Table II shows the five chamber concepts that were explored to alleviate the effects of cyclic stress and helium retention. "Laser/target issues" refers to laser propagation, accurate target placement, target warm-up during injection, and target injection velocity.

Having a vacuum in the chamber is attractive because simulations show that there are no issues with either target injection/survival [45] or laser propagation. Because of that, efforts were concentrated on the first two approaches. These will be discussed in this paper. Replaceable walls [48] were also considered, albeit less vigorously. Refer to the literature for work on issues for gas-filled chambers such as target survival, [45] chamber recovery, [49], and laser propagation [50]. A summary of these chamber concepts is provided in the literature [51].

For solid-wall chambers, our choice for the FW is a thin (∼1-mm) tungsten armor bonded to a low-activation ferritic steel substrate. This segregates the armor and structural functions. The tungsten was chosen to be thick enough to smooth the cyclic thermal stresses at the tungsten/steel interface, yet thin enough to ensure adequate heat removal before the next

TABLE II
REACTION CHAMBER CONCEPTS

	Concept (wall/chamber)	Advantages	Challenges
1	Solid wall/vacuum	Simplest Easier laser/target issues	Materials
2	Magnetic Intervention/vacuum	Smallest chamber Eliminates FW thermal load Eliminates He retention Minimal laser/target issues	Ion dumps
3	Replaceable solid wall/vacuum	Easier laser/target issues	Operational complexity
4	Solid wall/gas in chamber	Smaller chamber	Laser / target issues Chamber Recovery (hot gas and residual plasma)
5	Thick liquid walls	No materials issues (including neutronics)	Chamber Recovery Droplet formation Difficult to modify

pulse. We have deployed a number of facilities to mimic the threats onto this FW. The RHEPP facility at Sandia National Laboratories provides a source of repetitively pulsed high-energy ions [52]. A high-intensity infrared lamp at ORNL [53] mimics the cycle heat loading at the interface, and the Dragonfire laser facility at UCSD is used to precisely study the evolution of long-term cyclic heating of the armor [54]. These experiments are supported with the Unified Materials Response Code that is under development at UCLA and the University of Wisconsin [46], [55]. The objective is to develop a single tool to simulate all the relevant physics of the interaction between target emissions and the FW, including deposition, thermal stress, mechanical stress, helium migration, thermal transport, and long-term behavior.

The experiments for looking at cyclic thermal stress suggest an upper limit on the tungsten armor of 2400 °C. Below that, there is little evidence of long-term mass loss. Tungsten does exhibit some cracking, but the modeling suggests that these cracks relieve the localized mechanical stress and they should not propagate through to the substrate [46]. The experiments also show no long-term damage at the tungsten/steel interface. The 2400-°C limit can be met with the conventional target in an evacuated chamber with a radius of 11 m.

Helium retention was studied with a series of exposure experiments on the IEC electrostatic trap [56] at the University of Wisconsin. This produces full-power year (FPY) levels of helium fluence, but their energy represents only the lowest 5% of the prototypical helium energy spectrum. The experiments confirm that helium retention is a problem. The material quickly exfoliates and loses mass within the equivalent of a few days of full-power operation [57]. These results have been successfully modeled by UCLA [58]. However, newer research suggests two means to mitigate, if not downright prevent, helium exfoliation. One is based on the unique nature of helium implantation in an IFE system, and the other is the use of "nanoengineered" tungsten armor.

In an IFE system, helium is implanted in a short pulse into a wall that is rapidly heated. The wall then cools before the next shot. Given the relative immobility of helium clusters compared to monoatomic helium, the issue of studying prototypical

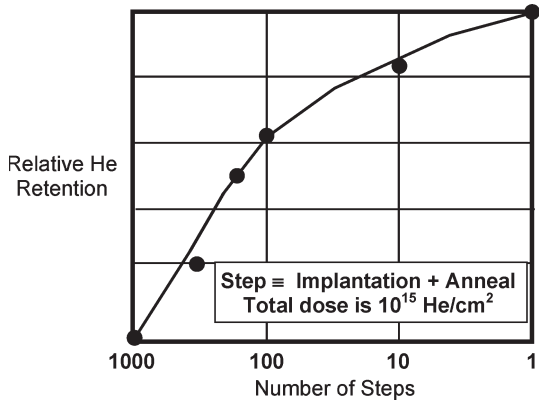

Fig. 14. Retained helium for different implantation histories.

implantation/anneal conditions may affect the relative retention of helium. The hypothesis was supported by simulations from UCLA [59] and a series of experiments at UNC Chapel Hill. [60]. In these experiments, a Van de graff Generator and rotating energy-degrader wheel generated helium ions with the prototypical target spectrum. Fig. 14 shows the amount of helium retained (as measured by the recoil proton spectrum) for three different implantation conditions into single-crystal tungsten. The implantation temperature was fixed at 850 °C, and the helium dose was fixed at 10^{15} He/cm^2 (an FPY is about 10^{20} He/cm^2). The dose was deposited in 1, 10, 100, and 1000 steps (1500 steps would be prototypical for this dose in a power plant). After each step, the sample was flash annealed to 2500 °C. The retained helium was measured with proton recoil spectroscopy.

The trend is to retain less helium wherein the number of steps is greater, which approaches the IFE prototypical implantation per pulse. However, other aspects are not prototypical: the time scales for implantation and subsequent heating are a few seconds long, the total fluence is only a small fraction of an FPY, and it is not practical to build an FW out of single-crystal tungsten. Nevertheless, the experiments suggest a potential method to deal with helium retention.

An additional and possibly more effective approach is to use a "nanoengineered" tungsten armor. The armor is made from

TABLE III
FRACTION OF RETAINED HELIUM FOR VARIOUS TUNGSTEN MORPHOLOGIES. 10^{16} He/cm^2 TOTAL DOSE, 100-STEP, AND 500-STEP IMPLANTATIONS

Dose steps	Single Crystal Tungsten	"Large Grain Size" Poly Crystalline Tungsten (10-15 microns)	"Small Grain Size" Poly Crystalline Tungsten (0.5 - 3 microns)	Nano Engineered tungsten (400-500 nm scale length)
100	74%	84%	63%	26%
500	N/A	81%	51%	15%

porous tungsten whose scale length is less than the helium migration distance (typically 50–100 nm). With this approach, the helium ions are slowed by the integrated mass of tungsten in their path, but wherever they finally come to rest, they are always close to the tungsten surface. Engineered structures have the added advantage of being more resistive to thermal cycling fatigue as tungsten can expand without restriction. Modeling supports this concept and also shows that thermal conduction to the substrate will not be an issue [61].

A series of experiments was performed with samples consisting of a solid tungsten undercoat and a porous tungsten topcoat. The porous tungsten was fabricated with a vacuum plasma spray process using 100-nm-size feedstock [62]. The first material produced had a scale length of 500 nm, which was larger than desired. Nevertheless, the implantation results showed evidence of lower helium implantation. The results are shown in Table III, which shows the percentage of retained helium for four different tungsten morphologies and a 100-step anneal cycle [63], [64]. In this case, the total dose was 10^{16} He/cm^2, which represents about 2 h of full-power operation. The retained helium was measured with proton recoil spectroscopy. The implanted helium was calculated from the measured accelerator current density and exposure time.

The data show that less helium is retained in tungsten with smaller grain size (or scale length). Postimplantation metrology corroborates this trend: Polycrystalline large-grain tungsten exhibits blistering at 2×10^{15} He/cm^2 and exfoliation at 10^{16} He/cm^2. In contrast, nanoengineered tungsten exhibits no surface changes at 5×10^{15} He/cm^2. The data in Table III also agree with the observation that less helium is retained with a larger number of implantation steps. Based on this, porous tungsten with scale sizes that are less than the 100-nm helium migration distance is expected to retain even less helium.

Further indications that nanoengineered tungsten may be the right approach were the results of recent helium implantation experiments with the University of Wisconsin electrostatic trap. Recall that this facility produces helium fluences that can exceed an FPY, but that the helium energy is only 30 keV and thus represents only the lower 5% of the spectrum. Fig. 15 shows the mass loss rate, as a function of helium implantation fluence, for the nanoengineered-tungsten-armored samples described earlier [65]. The fluence is also given as equivalent full-power days, assuming an 11-m-radius chamber and the conventional direct-drive target. The loss rate is rapid at first but slows considerably within the equivalent of 50 days. One interpretation is that the material is "adjusting" to a more

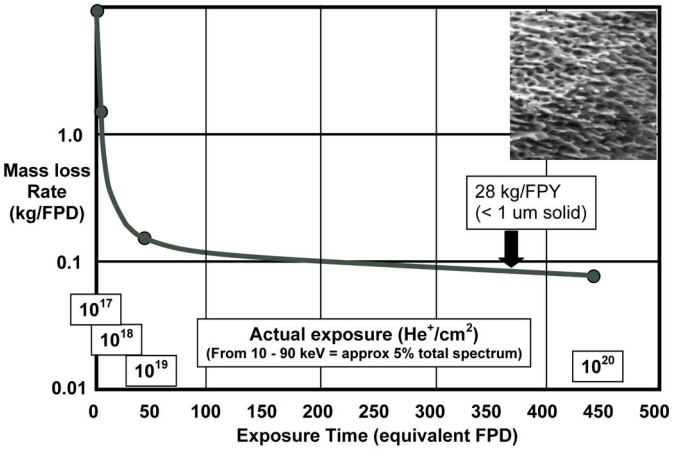

Fig. 15. Mass loss rate for the nanoengineered tungsten exposed to helium ions at prototypical fluences, and the lower 5% of the prototypical spectrum.

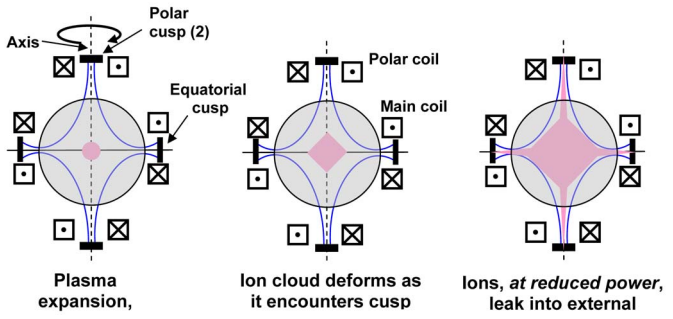

Fig. 16. Concept of magnetic intervention.

stable configuration. Another is that the early rapid loss may be due to other phenomena that are endemic to the system. That is being addressed. Nevertheless, the total material loss over the equivalent of 450 days of operation is only 1 μm of solid material.

Another consideration for the nanoengineered material is robustness to thermal cycling. A preliminary set of exposures on the Dragonfire laser facility show no detectable mass loss for up to 10^5 cycles if the peak temperature is kept below 2200 °C [66]. The material thermal response evolves during the first 10–20 min of exposure, which requires further study before definitive statements can be made. In light of these studies, nanoengineered tungsten, particularly if it can be made to the required 50–100-nm scale length, may lead to a solution for the FW.

It is entirely possible that a solid wall can never be made to withstand the direct emissions from the target. Although its simplicity warrants further exploration, prudence suggests adding other options. One appealing approach is based on magnetic intervention [67]. In this approach, a cusp magnetic field is imposed on the chamber and directs the ions through poloidal holes and an external belt. The ion energy is then absorbed in external dumps, thus isolating the energy absorption from the chamber. This process is shown schematically in Fig. 16.

The ions do not hit the chamber wall because their canonical angular momentum must be conserved. The ions are born at the chamber center, where the magnetic field and the radius of the ions are zero. Hence, their canonical angular momentum ($P_\theta = mru_\theta + (q/c)rA_\theta$) is also zero (here, r is the radius of the ion, m is the ion mass, $q = Ze$ is its charge, u_θ is the azimuthal component of velocity, and A_θ is the azimuthal component of vector potential which, due to the axial symmetry, is the only component of A). The canonical angular momentum must be conserved in the absence of collisions, which is the case here. As the magnetic field in a cusp arrangement increases with distance from the chamber center, the ions are confined to a region defined by $|A_\theta| \leq A^*$, where $A^* = muc/q$. As a result, the ions will never cross the field lines to hit the wall, and will leak out the poles and equatorial belt of the cusp.

Magnetic intervention has the following advantages.

1) The chamber radius can be much smaller and the choice of FW materials can be expanded because the wall only needs to absorb the energy of the X-rays, which carry just 1% of the reaction energy. As an example, consider a chamber of 5-m radius. If the FW is made of SiC (which has less X-ray stopping power and, hence, lower volumetric deposition), the surface temperature would increase by only about 130 °C.
2) A smaller chamber requires shorter distance for the injected target and, hence, a lower injection velocity. A 5-m-radius chamber requires only 50 m/s as opposed to over 100 m/s for an 11-m-radius solid-wall chamber. The lower velocity can readily be achieved by simple mechanical or magnetic injectors. Smaller chambers also require less placement accuracy.
3) The chamber can operate in vacuum, which facilitates chamber recovery for the next shot, assists accurate target placement (the most accurate target engagement bench tests were obtained with an evacuated system), and reduces target injection warm-up as the only heat load is radiation from the chamber wall.

The concept and key physics of magnetic intervention were demonstrated in a 1979 experiment at NRL, in which a pure deuterium plasma was formed in the center of the cusp geometry and allowed to leak out through the magnetic cusp [68]. The plasma was formed by dropping a deuterium pellet into the chamber, disassociating it with a CO_2 laser, and then ionizing it with an ND glass laser. This was arguably the first IFE experiment. The plasma showed no sign of instability and, based on magnetic probes, laser scattering, and witness plate measurements, was observed to exit the chamber through the cusps in a consistent well-defined pattern. Recent simulations have successfully modeled the motion of the plasma [69]. The codes used in those simulations are now being used to develop a magnetic-intervention-based chamber.

The challenge with magnetic intervention is dumping the ions. Even though the cusp magnetic field spreads the ions out in time, unless they are expanded onto an unrealistically large area, i.e., comparable to that of the chamber, the power per unit area incident on any surface is large. Thus, any solid surface would be quickly ionized, making recovery for the next shot problematic (we make the assumption that none of the dump material should be allowed back in the main chamber). Moreover, several species of ions are emitted, and none has a well-behaved energy distribution. For example, the hydrogen ions carry only 19% of the total energy, but their longer range requires almost ten times as much mass to be stopped. These considerations lead to situating the dump outside the chamber and absorbing the energy in a volume rather than a surface. This, in turn, implies an external cavity filled with vapor or mist. We have evaluated a number of configurations [70]. The most promising one uses additional coils to divert the ions that escape from the toroidal belt downward into an external dump region that is filled with gallium mist. The ions that exit the poles of the cusp are absorbed in tubes filled with the same gallium mist. The coils are configured so that the escaping plasma is outside the beam ports shown in Fig. 6. Energy absorption is a two-stage process. Some of the gallium absorbs the ion energy and is ionized and/or vaporized. The bulk of the gallium then cools the ions and vapor. The amount of gallium in the system is chosen so that the average temperature rise is less than 300 °C. Gallium is chosen because it is a liquid at slightly above room temperature, which alleviates start-up problems, and because it has very low vapor pressure (10^{-6} torr at 720 °C). The latter means that it will not interfere with laser propagation, target injection, target warm-up, or chamber recovery.

One consideration with magnetic intervention is that the polar field coils shown in Fig. 16 need to produce about 16 T on axis in order to minimize the ions that emanate from the poles. While these are relatively simple small-bore (10-cm) solenoidal coils and are within the state of the art [71], they are not routine items. The main coils are on the order of 0.75 T and are well within routine capabilities.

VIII. Auxiliary Systems

In addition to the key components listed previously, we have also produced conceptual designs for the other systems required for a power plant. We have several blanket designs for both magnetic intervention and conventional chambers [72]. These designs use either liquid FLIBE or PbLi as the breeder material and include the power conversion cycle. We have produced a conceptual design for a system to handle and process tritium, from recovering the unburned tritium in the chamber through reprocessing and purification to filling a new target [73], [74]. We have generated a conceptual design for the vacuum system that uses off-the-shelf components, costs under $20 million, and keeps the vacuum below 10^{-3} torr [75]. We have generated engineering concepts for the core of a laser IFE power plant [76] and undertaken a study to determine the feasibility of using

this approach to generate hydrogen. The study suggests that a Pb–17Li blanket, with a silicon carbide composite (SiC_f/SiC) structure operating at 1000 °C, could have more than 50% efficiency in generating hydrogen [77], [78]. The study assumes the hybrid sulfur cycle in which the final products are just hydrogen and oxygen. We have also generated costing models to help determine the economic effects of reactor size, target gain, laser cost, and repetition rate [79], [80].

IX. Next Step

This work is applicable to a wide range of approaches to laser fusion energy. One approach is the fusion–fission hybrid system in which a lower gain fusion target is surrounded by a fissile blanket to produce sufficient gain for a power plant. This is based on an extrapolation of present indirect-drive targets and a combination of NIF and Mercury laser technologies [81]. Another approach is to exploit the higher gain targets afforded by KrF to develop a pure-fusion energy system. NRL has proposed a three-stage program to develop a laser fusion energy power plant based on this approach [17]. The NRL program, based on the FTF or shock ignition targets shown in Fig. 1, would use a single FTF to develop the physics, technologies, integration issues, and the materials. As pointed out in the reference, that path could lead to the deployment of practical fusion power in far less time and with less risk than that in other approaches.

X. Conclusion

This paper has developed much of the scientific and technical bases needed for a power plant based on laser fusion energy. Credible approaches have been identified and are under development for virtually all the key components, including target physics, two types of lasers, final optics, target fabrication and engagement, reaction chambers, and auxiliary components. Where possible, these have been backed with experiments, bench demonstrations, and simulations. We are technically ready to take the next step to develop laser fusion energy.

Acknowledgment

The authors would like to thank the numerous scientists, technicians, engineers, programmers, support staff, and, most importantly, the over 40 students who contributed to and were awarded advanced degrees through the program presented in this paper.

References

[1] W. R. Meier and C. W. von Rosenberg, Jr, "Economic modeling and parametric studies for SOMBRERO—A laser-driven IFE power plant," *Fus. Technol.*, vol. 21, pp. 1552–1556, 1992.

[2] I. N. Sviatoslavsky, M. E. Sawan, R. R. Peterson, G. L. Kulcinski, J. J. MacFarlane, L. J. Wittenberg, H. Y. Khater, E. A. Mogahed, and S. C. Rutledge, "A KrF laser driven inertial confinement fusion reactor 'SOMBRERO'," *Fus. Technol.*, vol. 21, pp. 1470–1474, 1992.

[3] J. D. Sethian, M. Friedman, R. H. Lehmberg, M. Myers, S. P. Obenschain, J. Giuliani, P. Kepple, A. J. Schmitt, D. Colombant, J. Gardner, F. Hegeler, M. Wolford, S. B. Swanekamp, D. Weidenheimer, D. Welch, D. Rose, S. Payne, C. Bibeau, A. Baraymian, R. Beach, K. Schaffers, B. Freitas, K. Skulina, W. Meier, J. Latkowski, L.J. Perkins, D. Goodin, R. Petzoldt, E. Stephens, F. Najmabadi, M. Tillack, R. Raffray, Z. Dragojlovic, D. Haynes, R. Peterson, G. Kulcinski, J. Hoffer, D. Geller, D. Schroen, J. Streit, C. Olson, T. Tanaka, T. Renk, G. Rochau, L. Snead, N. Ghoneim, and G. Lucas, "Fusion Energy with Lasers, Direct Drive Targets, and Dry Wall Chambers," *Nucl. Fusion*, vol. 43, no. 12, pp. 1693–1709, 2003.

[4] A. J. Schmitt, J. W. Bates, S. P. Obenschain, S. T. Zalesak, D. E. Fyfe, and R. Betti, "Direct drive fusion energy shock ignition designs for sub-MJ lasers," *Fus. Sci. Technol.*, vol. 56, no. 1, pp. 377–383, Jul. 2009.

[5] S. E. Bodner, D. G. Colombant, A. J. Schmitt, J. H. Gardner, R. H. Lehmberg, and S. P. Obenschain, "Overview of new high gain target design for a laser fusion power plant," *Fusion Eng. Des.*, vol. 60, no. 1, pp. 93–98, Jan. 2002.

[6] A. J. Schmitt, D. G. Colombant, A. L. Velikovich, S. T. Zalesak, J. H. Gardner, D. E. Fyfe, and N. Metzler, "Large-scale high-resolution simulations of high gain direct-drive inertial confinement fusion targets," *Phys. Plasmas*, vol. 11, no. 5, pp. 2716–2722, May 2004.

[7] D. G. Colombant, A. J. Schmitt, S. P. Obenschain, S. T. Zalesak, A. L. Velikovich, J. W. Bates, D. E. Fyfe, and J. H. Gardner, "Direct-drive laser target designs for sub-megajoule energies," *Phys. Plasmas*, vol. 14, p. 056 317, 2007.

[8] R. Betti, C. D. Zhou, K.S. Anderson, L.J. Perkins, W. Theobald, and A.A. Solodov, "Shock ignition of thermonuclear fuel with high areal density," *Phys. Rev. Lett.*, vol. 98, no. 15, p. 155 001, Apr. 2007.

[9] R. Betti, A. A. Solodov, J. A. Delettrez, and C. Zhou, "Gain curves for direct-drive fast ignition at densities around 300 g/cc," *Phys. Plasmas*, vol. 13, no. 10, p. 100 703, Oct. 2006.

[10] R. H. Lehmberg and S. P. Obenschain, "Use of induced spatial incoherence for uniform illumination of laser fusion targets," *Opt. Commun.*, vol. 46, no. 1, pp. 27–31, 1983.

[11] R. H. Lehmberg and J. Goldhar, "Use of incoherence to produce to produce smooth and controllable irradiation profiles with KrF fusion lasers," *Fus. Technol.*, vol. 11, no. 3, pp. 532–541, 1987.

[12] S. Skupsky, R. W. Short, T. Kessler, R. S. Craxton, S. Letzring, and J. M. Soures, "Improved laser-beam uniformity using the angular dispersion of frequency-modulated light," *J. Appl. Phys.*, vol. 66, no. 8, p. 3456, 1989.

[13] S. Skupsky and R. S. Craxton, "Irradiation uniformity for high-compression laser-fusion experiments," *Phys. Plasmas*, vol. 6, no. 5, pp. 2157–2164, May 1999.

[14] R. H. Lehmberg and J. E. Rothenberg, "Comparison of optical beam smoothing techniques for inertial confinement fusion and improvement of smoothing by the use of zero-correlation masks," *J. Appl. Phys.*, vol. 87, no. 3, pp. 1012–1022, Feb. 2000.

[15] Jim Weaver, Private Communication.

[16] J. D. Sethian, M. Myers, J. L. Giuliani, Jr, F. Hegeler, M. Friedman, M. Wolford, D. Rose, D. Weidenheimer, D. Morton, and D. Giorgi, "Electra: A repetitively pulsed, electron beam pumped KrF laser to develop the technologies for fusion energy, Digest of Technical Papers," in *Proc. 15th IEEE Pulsed Power Conf.*, Monterey, CA, Jun. 2005, pp. 13–17.

[17] S. P. Obenschain, J. D. Sethian, and A. J. Schmitt, "Laser Based Fusion Test Facility," *Fus. Sci. Technol.*, vol. 56, no. 2, pp. 594–603, Aug. 2009.

[18] P. M. Burns, M. Myers, J. D. Sethian, M. F. Wolford, J. L. Giuliani, R. H. Lehmberg, M. Friedman, F. Hegeler, R. Jaynes, S. Abdel-Khalik, D. Sadowski, and K. Schoonover, "Electra: An Electron Beam Pumped KrF Rep-Rate Laser System for Inertial Fusion Energy," *Fus. Sci. Technol.*, vol. 56, no. 1, pp. 346–351, Jul. 2009.

[19] A. Bayramian, P. Armstrong, E. Ault, R. Beach, C. Bibeau, J. Caird, R. Campbell, B. Chai, J. Dawson, C. Ebbers, A. Erlandson, Y. Fei, B. Freitas, R. Kent, Z. Liao, T. Ladran, J. Menapace, B. Molander, S. Payne, N. Peterson, M. Randles, K. Schaffers, S. Sutton, J. Tassano, S. Telford, and E. Utterback, "The Mercury Project: A high average power, gas-cooled laser for inertial fusion energy development," *Fus. Sci. Technol.*, vol. 52, no. 3, pp. 383–387, Oct. 2007.

[20] C. Ebbers, J. P. Armstrong, A. J. Bayramian, G. Beer, R. W. Campbell, D. C. Chen, R. R. Cross, A. C. Erlandson, B. L. Freitas, G. Huete, R. K. Lanning, J. Menapace, W. A. Molander, N. Schenkel, K. I. Schaffers, S. B. Sutton, J. B. Tassano, S. Telford, E. Utterback, J. A. Caird, C. P. Barty, B. H. Chai, and Y. T. Fei, "Solid state lasers for fusion energy," in *Proc. 23rd Symp. Fusion Energy*, San Diego, CA, May 31–Jun. 5, 2009.

[21] A. Bayramian, J. Armstrong, G. Beer, R. Campbell, R. Cross, A. Erlandson, B. Freitas, J. Menapace, W. Molander, K. Schaffers, S. Sutton, J. Tassano, S. Telford, C. Ebbers, J. Caird, and C. Barty, "Progress in diode pumped solid state laser driver development for inertial fusion energy," in *Proc. 18th Topical Conf. Fusion Energy*, San Francisco, CA, Sep. 28–Oct. 2, 2008.

[22] D. Kehne, Private Communication.
[23] R. L. Bieri and M. W. Guinan, "Grazing incidence metal mirrors as the final elements in a laser driver for inertial confinement fusion," *Fus. Technol.*, vol. 19, pp. 673–678, May 1991.
[24] M. S. Tillack, S. A. Payne, N. M. Ghoniem, M. R. Zaghloul, and J. F. Latkowski, "Damage threats and response of final optics for laser-fusion power plants," in *Proc. Inertial Fusion Sci. Appl.*. Kyoto, Japan, Sep. 2001, pp. 717–721.
[25] M. S. Tillack and J. E. Pulsifer, "Long-Term Survival of Grazing-Incidence Metal Mirrors for Laser Fusion," *Fus. Sci. Technol.*, vol. 56, no. 1, pp. 446–451, Jul. 2009.
[26] A. J. Schmitt and J. H. Gardner, "Illumination uniformity of laser fusion pellets using induced spatial incoherence," *J. Appl. Phys.*, vol. 60, no. 1, pp. 7–13, Jul. 1986.
[27] M. W. McGeoch, "Port placement and illumination uniformity" *Proc. 12th HAPL Meeting*, Livermore, CA, Jun. 20, 2005. [Online]. Available: http://aries.ucsd.edu/HAPL/MEETINGS/0506-HAPL/08mcgeoch.ppt
[28] M. Sawan, A. Ibrahim, T. Bohm, and P. Wilson, "Nuclear assessment of shielding configuration options for final optics of HAPL laser fusion power plant," *Fus. Sci. Technol.*, vol. 56, no. 2, pp. 756–760, Aug. 2009.
[29] L. L. Snead, K. Leonard, J. Jellison, M. Sawan, and T. Lehecka, "Performance of dielectric mirrors for inertial fusion application," *Fus. Sci. Technol.*, vol. 56, no. 2, pp. 1069–1077, 2009.
[30] T. Lehecka, Private Communication.
[31] A. N. Mostovych, D. G. Colombant, M. Karasik, J. P. Knauer, A. J. Schmitt, and J. L. Weaver, "Enhanced Direct-Drive Implosions with Thin High-Z Ablation Layers," *Phys. Rev. Lett.*, vol. 100, no. 7, p. 075 002, 2008.
[32] B. A. Vermillion, B. W. McQuillan, L. C. Brown, D. T. Goodin, R. Paguio, J. E. Streit, D. G. Schroen, P. C. Goodman, and W. Maksaereekul, "Mass Production Methods for IFE Targets," *Fus. Sci. Technol.*, vol. 47, no. 4, pp. 1139–1145, Apr. 2005, AP-12.
[33] D. T. Goodin, N. B. Alexander, L. C. Brown, D. T. Frey, R. Gallix, C. R. Gibson, J. L. Maxwell, A. Nobile, C. Olson, R. W. Petzoldt, R. Raffray, G. Rochau, D. G. Schroen, M. Tillack, W. S. Rickman, and B. Vermillion, "A cost-effective target supply for inertial fusion energy," *Nucl. Fusion*, vol. 44, no. 12, pp. S254–S265, Dec. 2004.
[34] J. K. Hoffer, J. D. Sheliak, D. A. Geller, D. Schroen, and P. Ebey, "Beta-layering in foam-lined surrogate IFE targets," *Fus. Sci. Technol.*, vol. 50, no. 1, pp. 15–32, Jul 2006.
[35] A. S. Bozek, N. B. Alexander, D. Bittner, L. Carlson, T. J. Drake, G. W. Flint, D. T. Frey, D. T. Goodin, S. Grant, J. F. Hund, J. D. Kilkenny, R. W. Petzoldt, D. G. Schroen, R. W. Stemke, J. E. Streit, and B. A. Vermillion, "The production and delivery of inertial fusion energy power plant fuel: The cryogenic target," *Fusion Eng. Des.*, vol. 82, no. 15–24, pp. 2171–2175, Oct. 2007.
[36] K. J. Boehm, A. R. Raffray, N. B. Alexander, D. T. Frey, and D. T. Goodin, "Numerical and experimental analysis of using a fluidized bed as a prototypic mass production device for IFE target layering," *Fus. Sci. Technol.*, vol. 56, no. 1, pp. 422–426, Jul. 2009.
[37] N. Petta, T. Bernat, J. Karnes, and J. Streit, "Development of targets for inertial fusion energy: Current experiments and future power generation," in *Proc. 23rd Symp. Fusion Energy*, San Diego, CA, May 31–Jun. 5, 2009.
[38] J. J. Karnes, N. M. Petta, and J. E. Streit, "Optimization of phase transfer catalysis for in situ coating of resorcinol formaldehyde targets," *Fusion Sci. Technol.*, vol. 55, no. 4, pp. 472–476, May 2009.
[39] D. T. Goodin, J. F. Hund, R. R. Paguio, D. G. Schroen, A. Nikroo, R. W. Petzoldt, N. B. Alexander, L. Carlson, M. Tillack, K. Boehm, J. D. Sheliak, D. A. Geller, J. K. Hoffer, and G. Flint, "Progress in 'Demonstrating Feasibility of the Target Supply for Laser Fusion'," presented at the 18th Topical Conf. Fusion Energy, San Francisco, CA, Sep. 28–Oct. 2, 2008.
[40] D. Harding, "A concept for mass producing IFE targets," in *19th High Average Power Laser Program Workshop*, Oct. 22–23, 2008. [Online]. Available: http://aries.ucsd.edu/HAPL/MEETINGS/0810- HAPL/Day2/29%20HARDING%20Cryo%20Target%2023Oct0100davidhar.pdf
[41] D. R. Harding, D. H. Edgell, L. M. Elasky, R. Q. Gram, S. J. Verbridge, A. J. Weaver, M. D. Wittmaqn, and T. B. Jones, "Cryogenic targets for inertial confinement fusion experiments and future-energy applications," in *Proc. 23rd Symp. Fusion Energy*, San Diego, CA, May 31–Jun. 5, 2009.
[42] R. Petzoldt, N. Alexander, L. Carlson, G. Flint, D. T. Goodin, J. Spalding, and M. S. Tillack, "A continuous, in-chamber target tracking and engagement approach for laser fusion," *Fus. Sci. Technol.*, vol. 52, no. 3, pp. 454–458, Oct. 2007.
[43] L. Carlson, M. S. Tillack, T. Lorentz, N. Alexander, G. Flint, D. T. Goodin, and R. W. Petzoldt, "Improving the Accuracy of the Target Engagement Demonstration," *Fus. Sci. Technol.*, vol. 56, no. 1, pp. 409–416, Jul. 2009.
[44] L. J. Perkins, M. Tabak, C. Bibeau, R. Beach, A. Ladran, C. Barty, J. Harte, J. Sethian, A. Schmitt, R. Betti, and C. Zhou, *HAPL 13*, University of Rochester, Nov. 8–9, 2005. [Online]. Available:http://aries.ucsd.edu/HAPL/MEETINGS/0511-HAPL/Tuesday/05.0Perkins.ppt
[45] A. R. Raffray, "Threats, design limits and design windows for laser IFE dry wall chambers," *J. Nucl. Mater.*, vol. 347, no. 3, pp. 178–191, Dec. 2005.
[46] J. P. Blanchard and C. J. Martin, "Thermomechanical effects in a laser IFE first wall," *J. Nucl. Mater.*, vol. 347, no. 3, pp. 192–206, Dec. 2005.
[47] W. Wang, J. Roth, S. Lindig, and C. H. Wu, "Blister formation of tungsten due to ion bombardment," *J. Nucl. Mater.*, vol. 299, no. 2, pp. 124–131, Nov. 2001.
[48] M. E. Sawan, E. P. Marriott, C. S. Aplin, and L. L. Snead, "Mobile tiles for inertial fusion first wall/blanket," in *Proc. 23rd IEEE/NPSS SOFE (IEEE Cat. No. CFP09SOF-CDR)*, San Diego, CA, May 31–Jun. 5, 2009.
[49] Z. Dragojlovic and F. Najmabadi, "Effects of chamber geometry and gas properties on hydrodynamic evolution of IFE chambers," *Fus. Sci. Technol.*, vol. 47, no. 4, pp. 1152–1159, May 2005.
[50] J. A. Stamper, R. H. Lehmberg, T. Lehecka, A. V. Deniz, E. A. McLean, and J. D. Sethian, "Experimental studies of laser–target interactions in ambient gas, under IFE conditions," *Nucl. Fusion*, vol. 44, no. 7, pp. 745–751, Jul. 2004.
[51] J. P. Blanchard and R. Raffray, "Laser fusion chamber design," *Fusion Sci. Technol.*, vol. 52, no. 3, pp. 440–444, Oct. 2007.
[52] T. J. Renk, P. P. Provencio, T. J. Tanaka, C. L. Olson, R. R. Peterson, J. E. Stolp, D. G. Schroen, and T. R. Knowles, "Chamber wall materials response to pulsed ions at power-plant level fluences," *J. Nucl. Mater.*, vol. 347, no. 3, pp. 266–288, Dec. 2005.
[53] T. Hinoki, L. L. Snead, and C. A. Blue, "Development of refractory armored silicon carbide by infrared transient liquid phase processing," *J. Nucl. Mater.*, vol. 347, no. 3, pp. 207–216, Dec. 2005.
[54] F. Najmabadi, J. Pulsifer, and M. Tillack, "Update on armor simulation experiments at Dragonfire facility," in *Proc. 15th High Average Power Laser Program Workshop, General Atomics*, San Diego, CA, Aug. 8–9, 2006.
[55] J. P. Blanchard, Q. Hu, and N. Ghoniem, "A unified model for ion deposition and thermomechanical response in dry wall laser IFE chambers," *Fus. Sci. Technol.*, vol. 56, no. 1, pp. 341–345, Jul. 2009.
[56] S. J. Zenobia, R. F. Radela, B. B. Cipitia, and G. L. Kulcinski, "High temperature surface effects of He+ implantation in ICF fusion first wall materials," *J. Nucl. Mater.*, vol. 389, no. 2, pp. 213–220, May 2009.
[57] R. Radel and G. Kulcinski, "Effects of high temperature pulsed helium implantation on tungsten surface morphology," *Fus. Sci. Technol.*, vol. 52, no. 3, pp. 544–548, Oct. 2007.
[58] Q. Hu, S. Sharafat, and N. M. Ghoniem, "Modeling space–time dependent helium bubble evolution in tungsten armor under IFE conditions," *Fus. Sci. Technol.*, vol. 52, no. 3, pp. 574–578, Oct. 2007.
[59] S. Sharafat, A. Takahashi, Q. Hu, and N. M. Ghoniem, "A description of bubble growth and gas release of helium implanted tungsten," *J. Nucl. Mater.*, vol. 386–388, pp. 900–903, Apr. 2009.
[60] S. B. Gilliam, S. M. Gidcumb, D. Forsythe, N. R. Parikh, J. D. Hunn, L. L. Snead, and G. P. Lamaze, "Helium retention and surface blistering characteristics of tungsten with regard to first wall conditions in an inertial fusion energy reactor," *Nucl. Instrum. Methods Phys. Res. B, Beam Interact. Mater. At.*, vol. 241, no. 1–4, pp. 491–495, Dec. 2005.
[61] S. Sharafat, N. M. Ghoniem, M. Anderson, B. Williams, J. P. Blanchard, and L. L. Snead, "Micro-engineered first wall tungsten armor for high average power laser fusion energy systems," *J. Nucl. Mater.*, vol. 347, no. 3, pp. 217–243, Dec. 2005.
[62] S. O' Dell and R. Raffray, "Engineered Tungsten armor for dry wall IFE chambers," in *Proc. 14th High Average Power Laser Program Workshop*, Mar. 21–22, 2006. [Online]. Available: http://aries.ucsd.edu/HAPL/MEETINGS/0603-HAPL/Oral/29%20ODell–High%20Porosity%20Tungsten.ppt
[63] R. Parker, N. R. Parikh, R. G. Downing, S. O'Dell, G. Romanoski, T. Watkins, and L. Snead, "Helium retention in nano-porous tungsten implanted with helium threat spectrum mimicking IFE reactor conditions," in *Proc. 17th High Average Power Laser Program Workshop*, Oct. 30–31, 2007. [Online]. Available: http://aries.ucsd.edu/HAPL/MEETINGS/0710-HAPL/Presentation/10b.%20Parikh%20Implanted%20Ion%20Issues.ppt

[64] N. Parikh, R. Parker, R. Downing, L. Cao, and L. L. Snead, "High dose of helium implanted in nano-cavity tungsten to evaluate threshold of surface blistering due to He bubble formation," in *Proc. Amer. Nucl. Soc. Annu. Meeting*, Anaheim, CA, Jun. 8–12, 2008.

[65] S. Zenobia and G. Kulcinsi, "Retention and surface pore formation in helium implanted tungsten as a fusion first wall material," *Fus. Sci. Technol.*, vol. 56, no. 1, pp. 352–360, Jul. 2009.

[66] F. Najmabadi and L. Carlson, "Engineered material exposure in Dragonfire—A progress report," in *Proc. 19th High Average Power Laser Program Workshop*, Madison, WI, Oct. 22–23, 2008.

[67] Proposed by A. E. Robson.

[68] R. E. Pechacek, J. R. Greig, M. Raleigh, D. W. Koopman, and A. W. DeSilva, "Measurement of the plasma width in a ring cusp," *Phys. Rev. Lett.*, vol. 45, no. 4, pp. 256–259, Jul. 1980.

[69] D. V. Rose, E. A. Madrid, R. E. Clark, C. Thoma, D. R. Welch, A. E. Robson, J. D. Sethian, and J. L. Giuliani, "Magnetic intervention modeling," in *Proc. 18th High Average Power Laser Program Workshop*, Santa Fe, NM, Apr. 8–9, 2008. [Online]. Available: http://aries.ucsd.edu/HAPL/MEETINGS/0804-HAPL/Day1/8.Rose.ppt

[70] A. R. Raffray, A. E. Robson, J. Sethian, C. Gentile, D. Rose, and M. Sawan, "Laser IFE direct drive chamber concepts with magnetic intervention," *Fus. Sci. Technol.*, vol. 56, no. 1, pp. 333–340, Jul. 2009.

[71] H. J. Schneider-Muntau, "Large bore high field magnets," *Nucl. Phys. B—Proc. Suppl.*, vol. 72, pp. 152–163, Mar. 1999.

[72] A. R. Raffray, A. E. Robson, M. E. Sawan, G. Sviatoslavsky, I. N. Sviatoslavsky, and X. Wang, "A self-cooled liquid breeder blanket for a laser IFE power plant with magnetic intervention," *Fusion Sci. Technol.*, vol. 52, no. 3, pp. 603–608, Oct. 2007, and references therein.

[73] S. W. Langish, C. A. Gentile, T. Kozub, C. Priniski, J. Sethian, K. Sessions, B. Paul, L. Ciebiera, T. Dodson, and G. Gettelfinger, "IFE Power Reactor Plasma Exhaust Fuel Recovery System," presented at the 6th High Average Power Laser Program Workshop, Princeton, NJ, Dec. 12–23, 2006. [Online]. Available: http://aries.ucsd.edu/HAPL/MEETINGS/0612-HAPL/Presentation/Langish.ppt

[74] C. Gentile, T. Kozub, S. Langish, C. Pirinski, T. Dodson, F. Dahlgren, G. Gettlefinger, B. Paul, L. Ciebiera, K. Sessions, and J. Wermer, "Conceptual design of a plasma exhaust and fuel recovery system for an inertial fusion energy power reactor," presented at the Proc. 22nd Symp. Fusion Energy, Albuquerque, NM, Jun. 17, 2007.

[75] C. A. Gentile, C. Priniski, J. Sethian, W. Blanchard, L. Ciebiera, F. Dahlgren, G. Gettelfinger, C. Jun, and S. Langish, "Pumping IFE chambers," in *Proc. 13th High Average Power Laser Program Workshop*, Nov. 8–9, 2005. [Online]. Available: http://aries.ucsd.edu/HAPL/MEETINGS/0511-HAPL/Tuesday/09.0Gentile.ppt

[76] C. A. Gentile, F. Dahlgren, T. A. Dodson, T. A. Kozub, M. W. McGeoch, C. D. Priniski, A. R. Raffray, A. E. Robson, D. V. Rose, M. E. Sawan, J. D. Sethian, I. J. Zatz, H. Zhang, and the HAPL Team, "IFE direct drive reactor core and primary sub-system development," in *Proc. 18th Topical Conf. Fusion Energy,* San Francisco, CA, Sep. 28–Oct. 2, 2008.

[77] M. Gorensik, "Feasibility of hydrogen production using laser inertial fusion as the primary energy source," Savvanah River Nat. Lab., Aiken, SC, Savvanah River National Laboratory Report, WSRC-STI-2006-00221, Nov. 3, 2006.

[78] M. Gorensik, "Feasibility of hydrogen production using laser inertial fusion as the primary energy source," presented at the 16th High Average Power Laser Program Workshop, Princeton, NJ, Dec. 12–23, 2006. [Online]. Available: http://aries.ucsd.edu/HAPL/MEETINGS/0612-HAPL/Presentation/Gorensek.ppt

[79] W. R. Meier, "How does laser cost scaling effect the power plant design optimization?" presented at the 16th High Average Power Laser Program Workshop, Dec. 12–23, 2006. [Online]. Available: http://aries.ucsd.edu/HAPL/MEETINGS/0612-HAPL/Poster/MeierPoster.ppt

[80] W. R. Meier, Dec. 2008. unpublished report.

[81] E. Moses, "A sustainable nuclear fuel cycle based on laser inertial fusion energy," *Fus. Sci. Technol.*, vol. 56, no. 2, pp. 547–565, Aug. 2009.

Authors' photographs and biographies not available at the time of publication.